A Thin Film Viscoplastic Theory for Calving Glaciers: Toward a Bound on the Calving Rate of Glaciers

J. N. Bassis[1] and **L. Ultee[1]**

[1]Department of Climate and Space Science and Engineering, University of Michigan, Ann Arbor, MI, USA

Abstract Projections of the growth and demise of ice sheets and glaciers require physical models of the processes governing flow and fracture of ice. The flow of glacier ice has been treated using increasingly sophisticated models. By contrast, fracture, the process ultimately responsible for half of the mass lost from ice sheets through iceberg calving, is often included using ad hoc parameterizations. In this study we seek to bridge this gap by introducing a model where ice obeys a power law rheology appropriate for intact ice below a yield strength. Above the yield strength, we introduce a separate rheology appropriate for the flow of heavily fractured ice, where ice deformation occurs more readily along faults and fractures. We show that, provided the motion of fractured ice is sufficiently rapid compared to that of intact ice, the behavior of glaciers depends solely on the rheology of intact ice and the yield strength of ice and is insensitive to the precise rheology of fractured ice. Moreover, assuming that glacier ice is unyielded allows us to bound the long-term average rate of terminus advance, providing a first principles estimate of rates of retreat associated with the marine ice cliff instability. We illustrate model behavior using idealized geometries and climate forcing and show that the model not only exhibits realistic patterns of advance and retreat but also has the potential to exhibit hysteresis. This hysteresis could provide an explanation for the sudden onset of rapid retreat observed in marine-terminating glaciers.

1. Introduction

The Greenland ice sheet is surrounded by glaciers that terminate in near-vertical ice cliffs submerged in the ocean, called tidewater glaciers. Observations show that these marine-based margins in contact with both the atmosphere and ocean are most susceptible to rapid glacier change and radically increased mass loss (e.g., Benn et al., 2007; Bassis, 2011; Bassis & Walker, 2012; Rignot et al., 2011). Unlike melting, the other dominant contributor to ice sheet and glacier mass loss, iceberg calving—the process where blocks of ice detach from a glacier—can be very rapid and highly episodic (e.g., Howat et al., 2005, 2007; McFadden et al., 2011). Moreover, observations indicate that mass shed from the termini of Greenland's many tidewater glaciers is responsible for as much as half of annual mass loss from the ice sheet and that it drives patterns of thinning and acceleration deep inland from the coasts (Joughin et al., 2008; Rignot et al., 2011; Straneo et al., 2013).

Rapid disintegration is not limited to Greenland. In the early 1980s, Columbia Glacier, a tidewater glacier in Alaska, transitioned from a decade-long period of stability into a regime of rapid retreat characterized by more than 20 km of terminus retreat and hundreds of meters of thinning (Krimmel, 2001; Meier & Post, 1987; McNabb et al., 2012; O'Neel et al., 2005). More recently, DeConto and Pollard (2016) building on a theoretical model developed by Bassis and Walker (2012) have suggested that continued atmospheric warming could trigger a calving instability termed the "marine ice cliff instability", destabilizing large portions of West Antarctica with catastrophic consequences for sea level on decadal to century time scales. A similar instability has been invoked to explain Heinrich events—episodic disintegration events from the Laurentide Ice Sheet that sporadically discharged vast armadas of icebergs through the Hudson Strait into the North Atlantic (Bassis et al., 2017; Thomas, 1977).

Despite iceberg calving's pivotal role in the mass balance and dynamics of glaciers, it remains poorly understood, defying convenient parameterization in the large-scale numerical ice sheet/glacier models used for sea level rise projections (Benn et al., 2007). Attempts to parameterize the iceberg calving process have traditionally focused on formulating models for fractures, assuming that an iceberg will detach when either a surface or bottom crevasse penetrates the entire thickness or some critical fraction thereof (e.g., Benn

et al., 2007; Bassis & Ma, 2015; Nick et al., 2010; Rist et al., 2002; Weertman, 1980). These models can be tuned to successfully reproduce large-scale patterns of glacier retreat, but complications remain. For example, researchers typically focus on tensile failure, ignoring the potential for shear failure (Bassis & Walker, 2012; Bassis & Jacobs, 2013). Moreover, these models often use the depth of surface melt water filling surface crevasses as a tuning parameter that can be adjusted to match observations (e.g., Nick et al., 2010).

Alternatively, it is possible to describe fracture using a bulk phenomenological approach, such as continuum damage mechanics (e.g., Albrecht & Levermann, 2012; Borstad et al., 2012b; Duddu et al., 2013; Pralong & Funk, 2005). Damage mechanics models introduce a scalar (or occasionally tensor) damage variable that evolves in response to the stress field (e.g., Borstad et al., 2012b; Duddu et al., 2013; Pralong & Funk, 2005). Damage-based models are not limited by the instantaneous steady-state assumptions intrinsic to most fracture mechanics-based approaches and are able to account for the slow, progressive accumulation of damage. However, it remains unclear how to specify damage evolution; current theories either treat damage evolution heuristically or fit curves to limited laboratory experiments (e.g., Borstad et al., 2012a; Bassis & Ma, 2015; Borstad et al., 2016; Duddu et al., 2013; Pralong & Funk, 2005). More recently, discrete element models have been used to simulate the flow and fracture of highly fractured glacier ice (Astrom et al., 2014; Bassis & Jacobs, 2013). Granular models, unfortunately, are too computationally expensive to include in modern continental-scale ice sheet models and are primarily used to examine the shorter time scale processes associated with individual calving events.

The granular hypothesis of fractured ice sheet flow inherent in discrete element models is reminiscent of early theories of ice deformation based on plasticity theory in which the ice was assumed to deform only once the stress that exceeded a yield criterion (Cuffey & Paterson, 1994; Nye, 1957). In this study, instead of trying to explicitly incorporate the fracture of ice into a continuum model, we follow a suggestion recently proposed by Bassis and Jacobs (2013) and Bassis and Walker (2012) and attempt to explain patterns of glacier retreat by assuming that heavily fractured ice deforms more readily than intact ice along preexisting faults and fractures. Consistent with this hypothesis, we formulate a continuum model in which ice flows slowly like a power law fluid beneath a yield stress but fails above a critical yield strength, a type of approximation frequently used to simulate geological fractures within the framework of continuum mechanics (e.g., Dahlen, 1990; Moresi et al., 2003; O'Neill et al., 2006).

2. Outline of Paper

The bulk of this study is devoted to formulating and exploring the consequences of a newly proposed rheology for ice that allows ice to deform rapidly above a yield strength. The key hypothesis of this study (illustrated in Figures 3 and 5) is that ice has a yield strength, and above the yield strength, the effective viscosity of fractured ice is much lower than for intact ice. When the effective stress exceeds the yield strength, the fractured/yielded ice will deform rapidly exposing the boundary separating yielded and intact ice as the calving front. In this situation, the migration of the boundary separating intact and yielded ice will then describe the migration of the calving front. Readers uninterested in the mathematical exposition provided may want to skip to sections 6 and 7. It is in these sections where we derive a bound on calving rates associated with the marine ice cliff instability and provide more concrete examples of how the bound can be implemented in numerical ice sheet/glacier models. The paper is structured as follows: In section 3 we start by presenting the newly proposed biviscous rheology and nondimensionalization scheme used to make approximations. Next, in section 4, we proceed by making the thin film approximation to derive the equivalent to the usual "shallow ice" and "shallow shelf" approximations appropriate for our yield strength-dependent rheology. In section 5, we examine the limiting case when the state of stress within the glacier first approaches the yield strength of ice. In this limiting case, our model reproduces the perfect plastic approximation previously examined by Ultee and Bassis (2016). Moreover, we show that in the perfect plastic approximation, the yield strength of ice provides a boundary condition on the ice thickness at the terminus. In section 6 we build on the results from section 5 and show that provided that the effective viscosity of yielded ice is small compared to the effective viscosity of intact ice, the effective stress everywhere must always be less than the yield strength of ice. Crucially, this provides a bound on the ice thickness at the terminus identical to the bound provided by Bassis and Walker (2012) see section 5.1 of this manuscript. Moreover, we show that the inequality on the ice thickness near the terminus can be manipulated to provide a long-term bound on the calving rates of glaciers (section 6.2 and equation (55)). Our bound on the
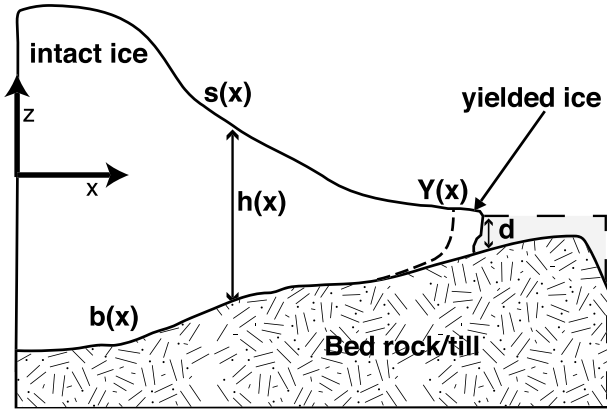
Figure 1. Sketch showing the coordinate system and geometry assumed. A yield surface $Y(x)$ is also shown which is initially quasi-parallel to the bed but rises and connects with the surface near the calving front.

retreat rate, unlike the empirical parameterization proposed by DeConto and Pollard (2016), depends on the glacier geometry (ice thickness, bed slope, and gradient in ice thickness) and climate forcing. Finally, in section 7, we provide some numerical examples to illustrate model behavior.

3. Model Description

3.1. Governing Equations

Denoting the fluid velocity and pressure fields by $(u(x, z, t), w(x, z, t))$ and $p(x, z, t)$, respectively, conservation of mass and momentum can be expressed in two dimensions as follows (Figure 1):

$$\rho(u_t + uu_x + wu_z) = -p_x + \partial_x \tau_{xx} + \partial_z \tau_{xz}, \tag{1a}$$

$$\rho(w_t + uw_x + ww_z) = -p_z + \partial_x \tau_{xz} - \partial_z \tau_{xx} - \rho g, \tag{1b}$$

$$u_x + w_z = 0, \tag{1c}$$

where ρ is the density of ice (910 kg/m^3) and g is the acceleration due to gravity (9.8 m/s^2). In the equations above, we denote partial derivatives with italic subscripts except when used to denote components of the deviatoric stress tensor (τ_{xx}, τ_{xz}), and we denote partial derivatives of deviatoric stress components by ∂_i. Components of the strain rate tensor are given by

$$\dot{\varepsilon}_{ij} = \frac{1}{2}\left(\frac{\partial u_i}{\partial x_j} + \frac{\partial u_j}{\partial x_i}\right), \tag{2}$$

allowing us to define the second invariant of the strain rate

$$\dot{\gamma} = \sqrt{\dot{\varepsilon}_{xx}^2 + \dot{\varepsilon}_{xz}^2}. \tag{3}$$

3.2. Rheology

Traditionally, a power law creep rheology called Glen's law is invoked to describe the flow of ice (e.g., Cuffey & Paterson, 1994). However, both laboratory and field observations (e.g., Schulson, 2001; Schulson & Duval, 2009; Vaughan, 1993) find that ice undergoes brittle failure when stress exceeds a critical value called the yield strength. Brittle failure permits motion along newly formed (or preexisting) faults and fractures within the ice, resulting in an abrupt increase in deformation rates. To accommodate this behavior, we consider a constitutive relationship that generalizes Glen's flow law such that glacier deformation only follows the usual power law creep relationship for stresses up to a yield strength τ_y. When stress exceeds the yield strength, we assume that enhanced deformation along preexisting fractures and faults results in a much smaller effective viscosity. We (crudely) approximate this behavior as power law creep with effective viscosity much lower than that of intact ice. Using subscripts (i, j) to denote coordinates (x, z), our biviscous rheology can be expressed in the form

$$\tau_{ij} = \begin{cases} B_i \, \dot{\gamma}^{\frac{1}{n}-1} \, \dot{\varepsilon}_{ij} & \text{for } \tau < \tau_y \\ \frac{1}{\dot{\gamma}}\left(B_f \, \dot{\gamma}^{1/n} + \left(1 - \frac{B_f}{B_i}\right)\tau_y\right) \dot{\varepsilon}_{ij} & \text{for } \tau \geq \tau_y, \end{cases} \tag{4}$$

where $(B_i, \, B_f)$ represent the rheological hardness parameters for intact and yielded ice, respectively, $\tau = \sqrt{\tau_{xx}^2 + \tau_{xz}^2}$ denotes the effective stress (in two dimensions), and n is the flow law exponent for ice (typically 3). Effectively, equation (4) defines an abrupt transition from an intact ice rheology to a much weaker failed—or yielded—rheology, similar to what is observed in laboratory experiments (Schulson, 2001; Schulson & Duval, 2009). The region of transition from unyielded to yielded ice is called a yield surface, and components of the stress and strain rate tensors (along with their invariants) are continuous across the yield surface.

The advantage of the biviscous approach is that it reduces to the power law rheology conventionally used by ice sheet modelers when the stress is beneath the yield strength but accounts for rapid deformation of
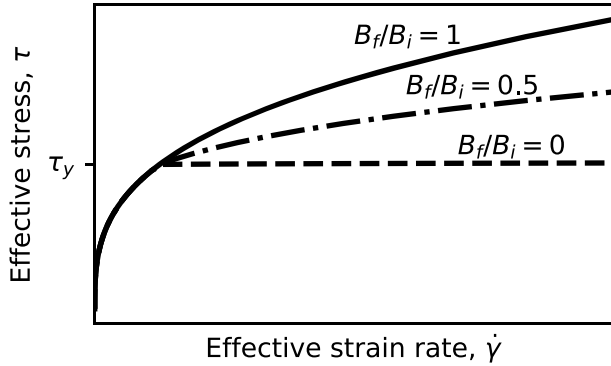
Figure 2. Diagram illustrating the biviscous rheology for various values of the ratio of hardness of intact and yielded ice. When the ratio $B_f/B_i = 1$, yielded ice has the same effective viscosity as intact ice, and power law creep continues at the same rate above the yield strength. When the ratio $B_f/B_i < 1$, there is an abrupt transition at the yield strength to a smaller ice hardness that results in a smaller increase in effective stress for a given increase in effective strain rate. As the ratio B_f/B_i approaches zero, ice behaves like a power law creeping material up until the yield strength, τ_y, at which point the effective stress can no longer increase and ice behaves like a plastic material.

fractured ice above the yield strength. This transition from intact to failed ice is analogous to damage mechanics, except that here, the transition to failed ice occurs instantaneously instead of over a time scale determined by a heuristic damage production function (e.g., Duddu et al., 2013; Pralong & Funk, 2005). In the absence of data to better constrain the rheology of yielded ice, we focus our mathematical exposition on the simple biviscous rheology defined by equation (4) as a limiting case. We treat B_i and B_f as constant parameters, ignoring any temperature dependence.

Figure 2 illustrates effective stress and strain rate for three cases of the biviscous rheology, distinguished by different values of the ratio B_f/B_i. As B_f/B_i tends toward zero, the effective stress is limited by the yield strength. This special case generalizes the perfect plastic rheology proposed by Ultee and Bassis (2016) and Nye (1957) such that unyielded ice is allowed the usual power law creep deformation rather than assumed to be rigid.

3.3. Boundary Conditions

Denoting the surface and bottom elevation of the glacier by $s(x,t)$, and $b(x)$, respectively, we apply the usual kinematic boundary condition $s_t + us_x = w + \dot{a}$ at the surface, where the accumulation rate $\dot{a}$ measures the net rate at which mass is added or removed from the glacier surface (units of meters of ice equivalent per unit time). We also impose the condition that the upper surface of the glacier is traction free, neglecting the small gradients in atmospheric pressure over the ice sheet
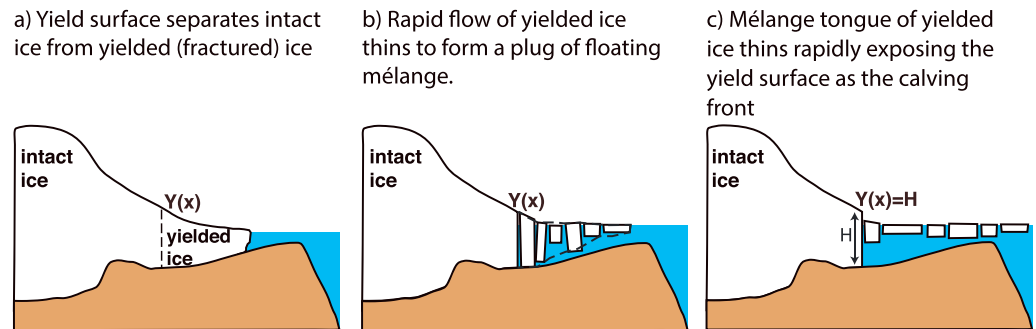
$$\left.\begin{array}{c}(\tau_{xx} - p)\,s_x = \tau_{xz} \\ \tau_{zz} - \tau_{xz}s_x = p\end{array}\right\} z = s(x,t). \tag{5}$$

At the base of the ice, we impose a no-penetration boundary condition, resulting in the requirement that $ub_x = w$, neglecting the (small) freezing/melting that can occur beneath grounded glaciers. Defining the basal shear traction

$$\tau_{\|} = -\frac{2\tau_{xx}b_x + (1 - b_x^2)\tau_{xz}}{1 + b_x^2}, \tag{6}$$

we assume that basal sliding only occurs when $|\tau_{\|}|$ exceeds the yield strength of the bed τ_b. This sliding law allows the bed to transition between frozen (no slip) and sliding. Thus, at $z = b(x,t)$ we impose

$$\tau_{\|} = \tau_b \frac{u_{\|}}{|u_{\|}|} + \beta^2 \left|u_{\|}\right|^{m-1} u_{\|}, \qquad \left|\tau_{\|}\right| \geq \tau_b, \tag{7}$$

a) Yield surface separates intact ice from yielded (fractured) ice

b) Rapid flow of yielded ice thins to form a plug of floating mélange.

c) Mélange tongue of yielded ice thins rapidly exposing the yield surface as the calving front

Figure 3. Schematic illustrating the boundary between intact and yielded ice. (a) An initial condition that consists of intact and yielded ice separated by a yield surface denoted by $Y(x)$. (b) Deformation of yielded ice concentrated along fractures and faults forming a yielded ice mélange. The yielded rheology simulates the bulk effect of fractures and bergs, conceptually illustrated with the dashed line in panel (b). (c) The end state after the yielded plug of mélange has rapidly deformed and been exported away exposing the yield surface as the calving front. The transition from panel (a) to panel (b) is paced by the characteristic time of the system and occurs nearly instantaneously if yielded ice deforms much faster than intact ice.

$$u = w = 0, \qquad \left| \tau_\| \right| < \tau_\mathrm{b}, \tag{8}$$

where $u_\| = (u + wb_x)/\sqrt{1 + b_x^2}$ is the component of ice velocity tangent to the bed, β an empirical sliding parameter, and m the sliding law exponent. This sliding law splices together a Weertman-type sliding law with a plastic sliding law (e.g., Cuffey & Paterson, 1994). We recover the Weertman-type sliding law in the limit that τ_b vanishes and the plastic sliding law when β tends to zero.

Finally, we assume a near-vertical calving face at $x = L(t)$ where we require continuity of traction at the ice-air and ice-water portions of the interface

$$\left. \begin{matrix} \tau_{xx} - p = \rho_\mathrm{w} g \langle z \rangle \\ \tau_{xz} = 0 \end{matrix} \right\} x = L(t). \tag{9}$$

Here the angle brackets are defined such that $\langle f \rangle = 0$ when $f \geq 0$ and $\langle f \rangle = f$ when $f < 0$. We take $z = 0$ to represent mean sea level.

There are three flow regimes of interest. The first flow regime corresponds to the flow of intact ice where the effective stress is everywhere less than the yield strength of ice. This regime is appropriate for the flow of glaciers that lack active calving margins. The second flow regime occurs when the stress invariant exceeds the yield strength so that the entire glacier is yielded (disarticulated flow of mélange). The third flow regime, illustrated in Figure 3, corresponds to a situation where the stress invariant at the calving front is perched at the yield strength, permitting both the flow of intact ice in the interior and active calving along the ice-ocean interface. It is this third flow regime that is most relevant for calving glaciers and the one we focus on here.

3.4. Nondimensionalization

We define a characteristic ice sheet thickness H_0 and horizontal length L_0. We scale the velocity components, u and w, by U_0 and $H_0 U_0 / L_0$, respectively, and scale time by L_0 / U_0. We then set

$$x = L_0 \tilde{x}, \quad z = H_0 \tilde{z}, \quad h = H_0 \tilde{h}, \quad b = H_0 \tilde{b}, \quad t = (L_0 / U_0) \tilde{t}, \quad \dot{a} = (H_0 U_0 / L_0) \tilde{\dot{a}}$$

$$\tau_{xz} = \beta^2 U_0^m \tilde{\tau}_{xz}, \quad \tau_{xx} = B_\mathrm{i} (U_0/L_0)^{1/n} \tilde{\tau}_{xx}, \quad \tau_{zz} = B_\mathrm{i} (U_0/L_0)^{1/n} \tilde{\tau}_{zz}, \quad p = \rho g H_0 \tilde{p},$$

$$\gamma = \frac{U_0}{L_0} \tilde{\gamma}, \quad \tau = \beta^2 U_0^m \tilde{\tau},$$

where the tilde indicates dimensionless variables. We also define the dimensionless yield strength $T_\mathrm{y} = \tau_\mathrm{y} L_0 / (\rho g H_0^2)$ and dimensionless basal yield strength $T_\mathrm{b} = \tau_\mathrm{b} L_0 / (\rho g H_0^2)$.

To ease the expansion, we set $\beta^2 U_0^m = \rho g H_0^2 / L_0$, anticipating that stresses associated with sliding are order unity for calving glaciers. With these definitions the model dynamics depend on three dimensionless numbers

$$\epsilon = \frac{H_0}{L_0}, \quad \nu = \frac{B_\mathrm{f}}{B_\mathrm{i}}, \quad \delta = \frac{B_\mathrm{i} \left(U_0/L_0 \right)^{1/n}}{\rho g H_0}. \tag{10}$$

The aspect ratio ϵ is small for all cases we consider here. The viscosity ratio ν, also assumed to be small for our analysis, compares the characteristic hardness of yielded and unyielded ice. The parameter δ is the ratio of the longitudinal deviatoric stress to the hydrostatic pressure and will be large or small, depending on the relative magnitude of basal friction and longitudinal stresses. We also define the dimensionless Reynolds number, $Re = U_0^2 L_0^2 / (g H_0^3)$. The Reynolds number may become large during the quasi-rigid body detachment of icebergs, but over the typically longer time scales associated with the evolution of glaciers and ice sheets, we anticipate that Re will remain order unity or less.

Nondimensionalizing and dropping the tilde decoration, the incompressibility condition remains the same, and the conservation of momentum equations become

$$\epsilon^2 Re \left(u_t + u u_x + w u_z \right) = -p_x + \delta \partial_x \tau_{xx} + \partial_z \tau_{xz}, \tag{11a}$$

$$\epsilon^4 Re (w_t + u w_x + w w_z) = -p_z + \epsilon^2 \partial_x \tau_{xz} - \delta \partial_z \tau_{xx} - 1, \tag{11b}$$

So long as $\epsilon^2 Re$ remains small, as expected for long time scales, we can neglect the inertial terms on the left-hand side of equations (11a) and (11b).

The dimensionless deviatoric stress and strain rate invariants become

$$\tau = \sqrt{\frac{\delta^2}{\epsilon^2}\tau_{xx}^2 + \tau_{xz}^2}, \quad \dot{\gamma} = \frac{1}{\epsilon}\sqrt{\epsilon^2 u_x^2 + \frac{1}{4}\left(u_z + \epsilon^2 w_x\right)^2}. \tag{12}$$

Recalling the dimensionless yield strength $T_y = \tau_y L_0/(\rho g H_0^2)$, the biviscous rheology can be written as

$$\left.\begin{array}{l} \tau_{xx} = \dot{\gamma}^{1/n-1} u_x \\ \tau_{xz} = \frac{1}{2}\frac{\delta}{\epsilon^2}\dot{\gamma}^{1/n-1}\left(u_z + \epsilon^2 w_x\right) \end{array}\right\} \tau < T_y \tag{13}$$

and

$$\left.\begin{array}{l} \tau_{xx} = \left[(1-\nu)\frac{\epsilon}{\delta}\frac{T_y}{\dot{\gamma}} + \nu\dot{\gamma}^{1/n-1}\right]u_x \\ \tau_{xz} = \frac{1}{2\epsilon}\left[(1-\nu)\frac{T_y}{\dot{\gamma}} + \nu\frac{\delta}{\epsilon}\dot{\gamma}^{1/n-1}\right]\left(u_z + \epsilon^2 w_x\right) \end{array}\right\} \tau \geq T_y. \tag{14}$$

The surface boundary conditions at $z = s(x, t)$ become:

$$\left(\delta\tau_{xx} - p\right)s_x = \tau_{xz}, \tag{15a}$$

$$-\epsilon^2\tau_{xz}s_x + \delta\tau_{zz} = p. \tag{15b}$$

With the aid of the dimensionless basal traction vector

$$\tau_\parallel = \frac{-2\delta\tau_{xx}b_x + (1 - \epsilon^2 b_x^2)\tau_{xz}}{1 + \epsilon^2 b_x^2}, \tag{16}$$

the basal boundary conditions of equations (7) and (8) become $u = w = 0$ for $\tau_\parallel < T_b$ and

$$\tau_\parallel = \left(\frac{T_b}{|u_\parallel|} + \left|u_\parallel\right|^{m-1}\right)u_b, \qquad \tau_\parallel \geq T_b, \tag{17}$$

with $u_\parallel = (u + \epsilon^2 w b_x)/\sqrt{1 + \epsilon^2 b_x^2}$.

At the calving front, the condition $\tau_{xz} = 0$ remains the same, but the nondimensional version of the longitudinal stress component of the calving front boundary condition applied at $x = L(t)$ can now be written as

$$\delta\tau_{xx} - p = \frac{\rho_w}{\rho}\langle z\rangle, \quad x = L(t). \tag{18}$$

4. Thin Film Approximation
4.1. Preliminaries
The thin film approximation proceeds by dropping terms of $\mathcal{O}(\epsilon)$ or smaller from equations (10)–(18). Equations (11a) and (11b) become

$$\delta\partial_x\tau_{xx} + \partial_z\tau_{xz} = p_x, \tag{19a}$$

$$-\delta\partial_z\tau_{xx} = p_z + 1. \tag{19b}$$

Integrating equation (19b) over the ice thickness and applying the surface boundary condition, defined by equation (15b), we find that to $\mathcal{O}(\epsilon^2)$,

$$p = (s - z) - \delta\tau_{xx}. \tag{20}$$

We can use equation (20) to simplify the boundary condition at $x = L(t)$. We still require $\tau_{xz} = 0$, but substituting equation (20) into equation (18) and integrating over the depth, we obtain a force balance condition that must be satisfied at the calving front (e.g., Van der Veen, 1999)

$$\delta\bar{\tau}_{xx} = \frac{h}{4}\left(1 - \frac{\rho_w}{\rho}\frac{d^2}{h^2}\right) = \frac{h}{4}\left(1 - r^2\right), \quad x = L(t), \tag{21}$$

where $\bar{\tau}_{xx}$ denotes the depth-averaged longitudinal deviatoric stress, h is the ice thickness, and d is the depth from the surface of the ocean to the bottom of the glacier (Figure 1) with $r^2 \equiv \rho_w d^2/(\rho h^2)$. Equation (21) provides the form of the boundary condition to be enforced at the calving front in "shallow" models.

Standard integration of the continuity equation and application of kinematic boundary conditions further yield an evolution equation for ice thickness

$$H_t + Q_x = \dot{a}, \tag{22}$$

where the ice flux $Q = \int_b^s u \, dz$.

Just as for traditional ice sheet models, the limits $\delta \ll 1$ and $\delta \sim 1$ correspond to important limiting cases of the dynamics. As we show next, $\delta \ll 1$ corresponds to the viscoplastic equivalent of the "shallow ice approximation" (SIA) used to simulate glaciers where vertical shear stresses dominate the force balance. In contrast, $\delta \sim 1$ corresponds to the "shelfy stream approximation," (SSA) applied to rapidly sliding glaciers where longitudinal stresses play an important role in the force balance.

4.2. Small Horizontal Extensional Stresses

The first case we consider treats both ϵ and δ as small parameters ($\delta \ll 1$, $\epsilon \ll 1$). Small δ corresponds to a situation where the pressure gradient is primarily balanced by gradients in the vertical shear stress, implying that resistance from basal drag plays a dominant role in resisting flow. This includes the case of a glacier frozen to its bed. Here we shall find that, provided the viscosity ratio ν is small, the yield strength of ice limits the maximum ice surface slope, as in the perfect plastic approximation.

When $\delta \ll 1$ and $\epsilon \ll 1$, we find from equation (20) that pressure is hydrostatic. Anticipating that vertical shear dominates the flow regime, we pose an expansion of the form

$$u = u_0(x, z, t) + \epsilon u_1(x, z, t) + \ldots, \tag{23}$$

where the indices correspond to the order of ϵ in each term of the expansion. Dropping terms of order δ, we find from equation (12) that $\dot{\gamma}_0 = (2\epsilon)^{-1} |\partial_z u_0|$, $\tau = |\tau_{xz}|$, and upon using the traction-free surface boundary condition given by equation (15b), we can integrate equation (19a) to find

$$\tau_{0xz} = -s_x(s - z). \tag{24}$$

The maximum shear stress occurs at the bed and decreases toward the surface. Recalling equations (12) and (24), it is now apparent that to leading order the effective stress is $\tau = |s_x| (s - z)$. When $h|s_x| < T_y$, yielding does not occur and deformation occurs solely through slow creeping flow of intact ice. This, however, is precisely the SIA frequently used in ice sheet modeling (e.g, Greve & Blatter, 2009), albeit with a basal yield strength-dependent sliding law.

The horizontal velocity can be decomposed into a component due to sliding $\mathcal{U}$ and a component due to internal deformation of the ice $\mathcal{D}$ such that the total velocity u is given by $u_0 = \mathcal{U}_0 + \mathcal{D}_0$. Recalling equation (17), we can express the sliding velocity $\mathcal{U}$ in terms of the shear stress

$$\mathcal{U}_0 = 0, \qquad |s_x| \, h < T_b,$$
$$\mathcal{U}_0 = -\left(h \, |s_x| - T_b\right)^{1/m} \frac{s_x}{|s_x|}, \qquad |s_x| \, h \geq T_b. \tag{25}$$

Investigating the deformational component of the velocity, we follow Balmforth and Craster (1999) and define a yield surface, $Y(x, t)$, demarking the boundary between intact ice (above) and yielded ice (below)
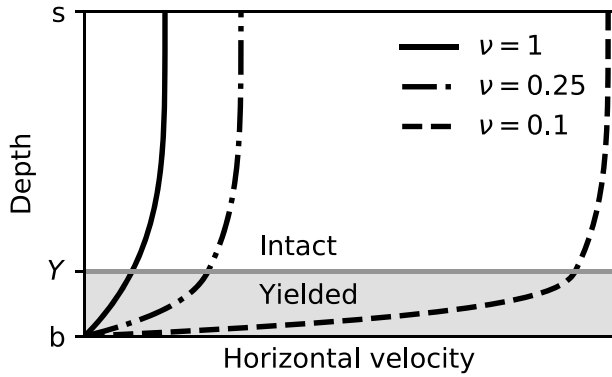
$$z = Y = \max \left(s - \frac{T_y}{|s_x|}, b(x) \right), \tag{26}$$

whence beneath the yield strength, deviatoric stresses take the leading order form

$$\tau_{0xz} = \frac{\delta}{\epsilon^{\frac{1}{n}+1} 2^{1/n}} |\partial_z u_0|^{\frac{1}{n}-1} \partial_z u_0. \tag{27}$$

Above the yield strength, the stresses are slightly more complex with leading order form

$$\tau_{0xz} = \left[(1 - \nu) \frac{T_y}{|\partial_z u_0|} + \nu \frac{\delta}{\epsilon^{\frac{1}{n}+1}} \frac{|\partial_z u_0|^{\frac{1}{n}-1}}{2^{1/n}} \right] \partial_z u_0. \tag{28}$$

Figure 4. Illustration of the velocity profile above and below the yield surface Y as a function of the ratio of the hardness parameter of yielded to intact ice v. When $v = 1$, velocity follows the usual shallow ice approximation profile of creeping above and below the yield surface. As v becomes smaller, the weaker rheology of yielded ice results in rapidly increasing velocities in the yielded layer.

Here we have adopted the more cumbersome (∂_x, ∂_z) notation for partial derivatives to avoid confusing subscripts labeling the order of terms in the expansion with those indicating partial derivatives.

We can substitute equations (27) and (28) into equation (24) to find the deformational component of the glacier velocity. After performing the vertical integration, we find

$$\mathcal{D}_0 = -2\frac{\epsilon^{n+1}}{v^n \delta^n}\frac{|s_x|^{n-1}s_x}{n+1}\left\{\left[Y - b + v(s - Y)\right]^{n+1} - \left[Y - z + v(s - Y)\right]^{n+1}\right\} \tag{29}$$

in the yielded region $z \leq Y$ and

$$\mathcal{D}_0 = -2\frac{\epsilon^{n+1}}{v^n \delta^n}\frac{|s_x|^{n-1}s_x}{n+1}\left\{v^n\left[(s - Y)^{n+1} - (s - z)^{n+1}\right] + \left[(Y - b) + v(s - Y)\right]^{n+1} - v^{n+1}(s - Y)^{n+1}\right\} \tag{30}$$

in the intact region $z > Y$. The deformational velocity of intact ice is small unless $\delta \leq \epsilon^{1+\frac{1}{n}}$, whereas for failed ice, deformational velocity is small unless $v\delta \leq \epsilon^{1+\frac{1}{n}}$.

The characteristics of the vertical velocity profile are illustrated in Figure 4 for various values of v. Taking the limit $v \to 0$, that is, $B_f \ll B_i$, we recover the Herschel-Bulkley velocity profile in which the velocity field is plug like above the yield strength (see, e.g., Balmforth & Craster, 1999). However, inspecting equation (30), we see that the deformational velocity in the yielded portion diverges like v^{-n} (see also Figure 4). Removing this divergence requires that the yield surface Y coincide with the bottom of the glacier, whence $h|s_x| = T_y$ and $s_x = \pm T_y/h$ and we recover the perfect plastic approximation (Nye, 1957; Ultee & Bassis, 2016). We now see that when yielded ice flows much more rapidly than intact ice, the yield strength limits the magnitude of the slope of the ice sheet.

We have now completely determined the velocity field for the case of small horizontal extensional stresses, but have yet to satisfy the calving front boundary condition. From equations (27) and (28), we see that if τ_{xz} vanishes at the calving front, $\partial_z u_0$ must become $\mathcal{O}\left(\epsilon^2\right)$ or smaller and the velocity field becomes plug like. The velocity field can only become plug like if deformational velocities are negligible, which requires that, at least near the calving front, the glacier is intact with stresses less than or equal to the yield strength. An intact calving front, however, is inconsistent with an active calving margin for grounded glaciers. The calving front boundary condition can be satisfied for an active calving margin in two ways. First, it is possible to have a region near the calving front where the extensional stress becomes large and $\delta\tau_{xx}$ becomes order unity or larger. Second, it is possible that the stress invariant near the calving front is at the yield strength. We consider next the case where extensional stresses near the calving front are large (section 4.3) before examining the more subtle situation when the effective stress at the calving front is perched at the yield strength (section 5).

4.3. Large Horizontal Extensional Stresses

We next examine the case where there is little resistance to sliding. To this end, we treat δ as an $\mathcal{O}(1)$ parameter. In this regime, τ_{xz} is $\mathcal{O}(\epsilon)$ smaller than τ_{xx}, but horizontal gradients in τ_{xx} remain comparable to vertical gradients in τ_{xz}. The effective stress then becomes $\tau = \delta\epsilon^{-1}|\tau_{xx}|$, with components of deviatoric stress in the unyielded regime

$$\left.\begin{aligned}\tau_{xx} &= \dot{\gamma}^{1/n-1}u_x \\ \tau_{xz} &= \frac{\delta}{2\epsilon^2}\dot{\gamma}^{1/n-1}u_z\end{aligned}\right\}\tau < T_y \tag{31}$$

and in the yielded regime

$$\left.\begin{aligned}\tau_{xx} &= \left[(1-v)\frac{\epsilon}{\delta}\frac{T_y}{\dot{\gamma}} + v\dot{\gamma}^{\frac{1}{n}-1}\right]u_x \\ \tau_{xz} &= \left[(1-v)\frac{T_y}{\epsilon\dot{\gamma}} + v\frac{\delta}{\epsilon^2}\dot{\gamma}^{\frac{1}{n}-1}\right]\frac{1}{2}u_z\end{aligned}\right\}\tau \geq T_y. \tag{32}$$

To leading order in equations (31) and (32), we find $u_z \sim \mathcal{O}(\epsilon^2)$ and weak resistance to sliding results in plug flow (see, e.g., Greve & Blatter, 2009). This suggests an expansion of the form

$$u = u_0(x,t) + \epsilon^2 u_2(x,z,t) + \ldots, \tag{33}$$

where we have built in the leading order plug flow solution and we have again styled indices to reflect the order of terms in the expansion with respect to ϵ.

For stresses beneath the yield strength, the analysis parallels the SSA used to model glaciers where most of the resistance originates from a combination of sliding and horizontal stretching (c.f. Greve & Blatter, 2009). Integrating equation (19a) over the depth and applying the surface and basal boundary conditions yields an elliptic equation for velocity

$$2\delta \frac{\partial}{\partial x} \left(h \left| \frac{\partial u_0}{\partial x} \right|^{1/n-1} \frac{\partial u_0}{\partial x} \right) - \left(\frac{T_b}{|u_0|} + |u_0|^{m-1} \right) u_0 = h \frac{\partial s}{\partial x}, \tag{34}$$

equivalent to the usual SSA. The SSA is often used to simulate the rapidly flowing portion of glaciers and ice sheets, but is limited to intact ice.

The case where effective stress exceeds the yield strength is more interesting. Assuming that T_y remains order unity, we find using equations (32) and (33) that the deviatoric stress components $\tau_{0xx} = v|\partial_x u_0|^{\frac{1}{n}-1}\partial_x u_0$ and $\tau_{0xz} = \frac{v}{2}\delta|\partial_x u_0|^{\frac{1}{n}-1}\partial_z u_2$ are large compared to the yield strength. Using equation (20) in equation (19b) and integrating over the glacier thickness result in the momentum equation

$$2\delta v \frac{\partial}{\partial x} \left[h \left| \frac{\partial u_0}{\partial x} \right|^{1/n-1} \frac{\partial u_0}{\partial x} \right] - \left(\frac{T_b}{|u_0|} + |u_0|^{m-1} \right) u_0 = h \frac{\partial s}{\partial x}, \tag{35}$$

which can be combined with equation (22) to find

$$h_t + \frac{\partial(hu_0)}{\partial x} = \dot{a}. \tag{36}$$

These equations are analogous to the SSA (Greve & Blatter, 2009), but this regime corresponds to the flow of disarticulated ice above the yield strength. Equations (35) and (36) thus apply to failed ice, and this motion of heavily fractured ice may be analogous to the dynamics of the mixture of failed ice, icebergs, and sea ice called mélange that clogs many proglacial fjords. In this flowline model, however, buttressing from mélange could only arise in regions where bed protrusions provided resistance to flow. In more realistic, two-dimensional models, buttressing could also arise from shear stress along fjord margins.

In the limit $v \ll 1$, equation (35) reduces to

$$-\min \left(\frac{T_b}{|u_0|} + |u_0|^{m-1}, \frac{T_y}{|u_0|} \right) u_0 = hs_x. \tag{37}$$

The minimum arises because, as we saw in section 3.2, the basal shear stress cannot exceed the yield strength of ice in the small v limit. This regime overlaps with the vertical shear-dominant solution with the $\mathcal{O}(\epsilon^{n+1}/\delta^n)$ vertical shearing term omitted. In the small v limit, once the bed reaches the yield strength $s_x = \pm T_y/h$ and we again recover the perfect plastic approximation (Nye, 1957). However, the boundary condition at the calving front can be written in the form

$$\frac{\partial u_0}{\partial x} = \frac{1}{\delta^n v^n} \left[\frac{h}{4} \left(1 - r^2 \right) - \epsilon(1-v)T_y \right]^n, \tag{38}$$

and we see that with small v, either $\partial_x u_0$ must diverge or the two terms in square brackets in equation (38) must balance. Balancing these two terms requires that $\epsilon T_y \sim h(1-r^2)/4$, which provides a boundary condition on the ice thickness. It is this situation, where the effective stress is at the yield strength, that we examine next.

5. Limiting Dynamics: Onset of Flow at the Yield Stress and the Perfect Plastic Approximation

Our next goal is to examine the onset of yielding, where the effective stress in the glacier first approaches the yield strength. Recalling that the yield surface demarks the boundary between intact and yielded ice, we shall show that in this limiting case the yield surface is required to extend along the bottom of the glacier *and* through the calving front, corresponding to the perfect plastic approximation. An important result in this limit is that the yield condition provides a boundary condition on the ice thickness at the calving front analogous to one deduced by Bassis and Walker (2012).

To probe this limiting case, we assume that $\nu \ll 1$ (hardness of yielded ice is much smaller than the hardness of intact ice) and $\epsilon^{1/n+1} \leq \delta \ll 1$, corresponding to a glacier where sliding is rapid and vertical shear deformation can be neglected—realistic assumptions near the terminus of many calving glaciers. Anticipating that the flow will be plug like to leading order, we pose an expansion of the form

$$\hat{u} = \frac{1}{\epsilon}\hat{u}_0(x,t) + \hat{u}_1(x,z,t) + \ldots, \tag{39}$$

where the hat decoration is used to distinguish the expansion in this regime from the shallow ice and shallow shelf scalings considered previously. We have also built in the leading order plug flow solution by explicitly omitting the z dependence of the leading order $\hat{u}_0$ term. Moreover, anticipating that flow in the yielded regime is much faster than flow in the intact regime, we included a leading order term that is inversely proportional to ϵ to describe the large velocity increase at or above the yield strength. For small ϵ, the first term $\hat{u}_0(x,t)$ is much larger than $\hat{u}_1(x,z,t)$. Breaking with prior notation, subscripts labeling the terms in the expansion start at zero to avoid negative indices.

With these assumptions, the strain rate invariant is given by

$$\hat{\dot{\gamma}}_0 = \sqrt{\left(\frac{\partial \hat{u}_0}{\partial x}\right)^2 + \frac{1}{4}\left(\frac{\partial \hat{u}_1}{\partial z}\right)^2}. \tag{40}$$

For stresses beneath the yield strength, the rheology can be written as

$$\epsilon^{1/n}\hat{\tau}_{xx} = \hat{\dot{\gamma}}_0^{1/n-1}\partial_x\hat{u}_0, \tag{41a}$$

$$\frac{\epsilon^{1/n+1}}{\delta}\hat{\tau}_{xz} = \frac{1}{2}\hat{\dot{\gamma}}_0^{1/n-1}\partial_z\hat{u}_1, \tag{41b}$$

and to leading order we find $\partial_x\hat{u}_0 = \partial_z\hat{u}_1 = 0$. In this limit, the strain rates vanish beneath the yield strength, recovering the "rigid plastic" limit considered by Ultee and Bassis (2016) in which glacier ice passively thickens until the yield strength is reached.

Above the yield strength, the rheology can be written as

$$\hat{\tau}_{xx} = \left[(1-\nu)\frac{\epsilon}{\delta}\frac{T_y}{\hat{\dot{\gamma}}_0} + \frac{\nu}{\epsilon^{1/n}}\hat{\dot{\gamma}}_0^{1/n-1}\right]\frac{\partial\hat{u}_0}{\partial x}, \tag{42a}$$

$$\hat{\tau}_{xz} = \left[(1-\nu)\frac{T_y}{\hat{\dot{\gamma}}_0} + \frac{\nu\delta}{\epsilon^{1/n+1}}\hat{\dot{\gamma}}_0^{1/n-1}\right]\frac{1}{2}\frac{\partial\hat{u}_1}{\partial z}. \tag{42b}$$

If $\nu \ll 1$, equations (42a) and (42b) can be approximated as

$$\hat{\tau}_{xx} = \frac{\epsilon}{\delta}\frac{T_y}{\hat{\dot{\gamma}}_0}\frac{\partial\hat{u}_0}{\partial x}, \tag{43a}$$

$$\hat{\tau}_{xz} = \frac{T_y}{\hat{\dot{\gamma}}_0}\frac{1}{2}\frac{\partial\hat{u}_1}{\partial z}. \tag{43b}$$

Noting that the second stress invariant is

$$\hat{\tau} = \sqrt{\frac{\delta^2}{\epsilon^2}\hat{\tau}_{xx}^2 + \hat{\tau}_{xz}^2} = \frac{T_y}{\dot{\gamma}_0}\sqrt{\left(\frac{\partial \hat{u}_0}{\partial x}\right)^2 + \frac{1}{4}\left(\frac{\partial \hat{u}_1}{\partial z}\right)^2} = T_y,$$ (44)

we conclude that in the flow regime "above" the yield strength, the stress invariant is, in fact, perched at the yield strength. Therefore, at the onset of yielding, the effective stress is at the yield strength through the full ice thickness.

To order ϵ, we find

$$s_x = \pm\frac{T_y}{h},$$ (45)

and we see that this situation corresponds to the perfect plastic approximation. The horizontal velocity is determined by integrating the mass balance equation such that

$$\hat{u}_0 = \epsilon\left(\frac{1}{h(L)}\int_0^{x_L}(\dot{a} - h_t)\ dx\right),$$ (46)

and we have now recovered the perfect plastic approximation (Nye, 1957; Ultee & Bassis, 2016).

Because the effective stress reaches the yield strength throughout the ice thickness, satisfying the calving front boundary condition at $x = L(t)$ requires that the calving front is also a yield surface. The boundary condition defined by equation (21) is then

$$\epsilon T_y = \frac{h}{4}\left(1 - \frac{\rho_w}{\rho}\frac{d^2}{h^2}\right).$$ (47)

Consistently enforcing vanishing shear stress at the calving front along with the calving front boundary condition defined by equation (47) requires that the ice thickness h and vertical shear strain rate $\partial_z\hat{u}_0$ both become order ϵ or smaller and the asymptotic expansion breaks order—considered in Appendix A. Nonetheless, we anticipate from equation (47) that requiring the yield surface to extend through the calving front requires

$$h_L = h_y = 2\epsilon T_y + \sqrt{\frac{\rho_w d^2}{\rho} + 4\epsilon^2 T_y^2},$$ (48)

where h_y is the *required* terminus thickness and we have discarded the unphysical negative square root.

6. Simple Models of Calving Glaciers

In the previous section, we found that the perfect plastic approximation requires the yield surface demarking the boundary between intact and disarticulated ice to lie along the bed and the calving front. The assumption that ice is everywhere at the yield strength is, however, a very restrictive assumption. A less restrictive assumption is that the stress invariant at the bed must be less than the yield strength of ice. In this case, we use the rheology of intact ice. Focusing on rapidly sliding glaciers where the internal deformation of intact ice can be neglected, the dynamics are encompassed by the SSA defined by equation (34)

$$2\delta\frac{\partial}{\partial x}\left(h|u_x|^{1/n-1}u_x\right) - \min\left(\frac{T_b}{|u|} + |u|^{m-1}, \frac{T_y}{|u|}\right)u = hs_x.$$ (49)

In equation (49), we have dropped the order indices of equation (34) to ease notation, and the minimum in the basal shear traction arises because the basal shear stress cannot exceed the yield strength (section 4.2). With the assumption of intact glacier ice, we also impose the condition that ice thickness at the terminus $h_L = h(L(t), t)$ not exceed the yield thickness h_y, resulting in the inequality $h_L \leq h_y$. As we show next, this inequality serves as a boundary condition and allows us to deduce bounds on the calving rate of glaciers.

6.1. Bounds on the Calving Rate: Kinematics of Calving Front Evolution

Our goal is to derive an expression that describes the rate of terminus advance (or calving rate) appropriate for a glacier with terminus at—or beneath—the yield thickness. We start by taking the advective derivative of ice thickness at the terminus

$$\frac{Dh_{\mathrm{L}}}{Dt} = \frac{\partial h_{\mathrm{L}}}{\partial t} + \left(u - u_{\mathrm{c}}\right)\frac{\partial h}{\partial x}, \tag{50}$$

where $u\text{-}u_{\mathrm{c}}$ denotes the rate of advance of the terminus and u_{c} is the calving rate (units of length/time) associated with mass lost along the calving front. Next, we use the continuity equation in the form

$$\frac{\partial h}{\partial t} = \dot{a} - \frac{\partial u}{\partial x}h - \frac{\partial h}{\partial x}u \tag{51}$$

to eliminate $\partial h/\partial t$ from equation (50), providing a kinematic expression for the ice thickness at the calving front

$$\frac{Dh_{\mathrm{L}}}{Dt} = \dot{a} - \frac{\partial u}{\partial x}h - \frac{\partial h}{\partial x}u_{\mathrm{c}}. \tag{52}$$

The first term on the right-hand side of equation (52) denotes the accumulation rate at the terminus (often small and/or negative). The second term denotes the rate at which ice thickness decreases at the calving front due to dynamic thinning. The third term is an advective term associated with upstream migration of the calving front due to iceberg calving. Because ice thickness generally increases upstream ($h_x < 0$), the advective term usually acts to increase ice thickness at the calving front. Provided $h_x < 0$, the calving rate u_{c} changes the balance between dynamic thinning and advective thickening at the calving front, controlling whether the terminus thins or thickens. Equation (52), however, is a purely kinematic description and does not provide a means of specifying the calving rate u_{c}. To specify the calving rate, we must apply additional constraints.

6.2. Bounds on the Calving Rate: Yield Thickness Greater Than Flotation Thickness

Icebergs detach from calving glaciers, and this suggests that the stress invariant at the terminus of actively calving glaciers must be perched near the yield strength. Equation (48) translates this requirement to a constraint on ice thickness. Moreover, for grounded glaciers, the ice thickness also cannot be less than the flotation thickness $h_{\mathrm{f}} = \rho_{\mathrm{w}}d/\rho$. Provided that $h_{\mathrm{f}} \leq h_{\mathrm{y}}$, the terminus thickness is bounded above and below and $h_{\mathrm{f}} \leq h_{\mathrm{L}} \leq h_{\mathrm{y}}$. We treat the case $h_{\mathrm{f}} > h_{\mathrm{y}}$ in the next section.

Considering first glaciers with a calving front thickness perched at the yield thickness, we take the advective derivative of the yield thickness

$$\frac{Dh_{\mathrm{y}}}{Dt} = \left(u - u_{\mathrm{c}}\right)\frac{\partial h_{\mathrm{y}}}{\partial x} \tag{53}$$

and equate it to the advective derivative of ice thickness at the terminus defined by equation (52), where we have also assumed that the bed topography is fixed (or evolves slowly enough that the time derivative of the yield thickness h_{y} can be neglected). This allows us to uniquely determine the calving rate necessary to maintain the terminus at the yield thickness

$$u_{\mathrm{c}} = u_{\mathrm{y}} = u - \frac{\dot{a} - u\frac{\partial h}{\partial x} - h\frac{\partial u}{\partial x}}{\left(\frac{\partial h_{\mathrm{y}}}{\partial x} - \frac{\partial h}{\partial x}\right)}, \quad \text{when } h_{\mathrm{L}} = h_{\mathrm{y}}, \tag{54}$$

where we have assumed $(\partial_x h_{\mathrm{y}} - \partial_x h) \neq 0$ and u_{y} denotes the specific calving rate u_{c} required to maintain the ice thickness at the yield thickness h_{y}.

A similar calculation shows that if the ice thickness is required to remain at flotation, then the calving rate u_{f} necessary to maintain the calving front at buoyancy is given by

$$u_{\mathrm{c}} = u_{\mathrm{f}} = u - \frac{\dot{a} - u\frac{\partial h}{\partial x} - h\frac{\partial u}{\partial x}}{\left(\frac{\partial h_{\mathrm{f}}}{\partial x} - \frac{\partial h}{\partial x}\right)}, \quad \text{when } h_{\mathrm{L}} = h_{\mathrm{f}}. \tag{55}$$

Note that $\dot{x}_{\mathrm{g}} = u - u_{\mathrm{f}}$ is just the usual expression for grounding line migration (Schoof, 2007). However, the physical interpretation of equation (55) is that the calving front advances and thins to buoyancy before calving, analogous to the buoyant calving regime proposed for Helheim Glacier (e.g., Murray et al., 2015).

From equation (52), if the ice thickness is initially less than the yield thickness and the calving rate u_c is larger than u_y, then the ice thickness will increase until the yield strength is reached and equation (54) will become valid again. Hence, equation (54) bounds the long-term calving rate from above. Similarly, if the ice thickness is initially greater than the flotation thickness and the calving rate u_c is smaller than u_f, then the ice thickness will decrease until the flotation thickness is reached and equation (55) will become valid. Hence, equation (55) bounds the calving rate from below.

Formally, equation (54) is an *upper* bound and equation (55) is a *lower* bound on calving rate when $\partial_x h_Y - \partial_x h > 0$ (i.e., when ice thickness decreases toward the terminus and bed topography varies on a length scale that is large compared with ice thickness—see Appendix A). When $\partial_x h_Y - \partial_x h < 0$, the bounds are reversed.

At the onset of yielding, continuity of strain rate across the yield surface at the calving front requires

$$\frac{\partial u}{\partial x} = \frac{1}{\delta^n}\left[\frac{1}{4}h\left(1 - r^2\right)\right]^n. \tag{56}$$

So long as the ice thickness is known and we have a model capable of calculating the velocity at the terminus u, equations (54) and (56) provide a self-consistent means of estimating the calving rate (or rates of terminus advance). Together, these two limits suggest that long-term calving rates are constrained by the fact that the ice thickness must remain less than the yield thickness and greater than the flotation thickness. These bounds remain valid until the flotation thickness exceeds the yield thickness, which we consider next.

6.3. Bounds on the Calving Rate: Yield Thickness Less Than Flotation Thickness

For glaciers on retrograde beds, such as Pine Island and Thwaites glaciers grounded deep below sea level, retreat of the calving front will eventually result in an ice thickness where the flotation thickness exceeds the yield thickness of ice (Bassis & Walker, 2012). In these cases, we must use equation (35) to compute the velocity u for the portions of the glacier that are yielded. We can still use equation (55) to compute the calving rate associated with migration of the fully yielded terminus, which must now be at the flotation thickness. However, we must use the yielded rheology in computing the horizontal strain rate

$$\frac{\partial u}{\partial x} = \frac{1}{\nu^n \delta^n}\left[\frac{1}{4}h\left(1 - r^2\right)\right]^n. \tag{57}$$

Both the velocity and grounding line dynamics now depend on the viscosity of yielded ice via the hardness ratio ν. Despite poor constraints on the precise value of ν, in the plausible case that yielded ice is softer than intact ice ($\nu \ll 1$) and in the absence of stabilizing features, dynamic thinning and grounding line retreat in this regime could occur as catastrophic disintegration—perhaps analogous to the disintegration of the Larsen B ice shelf (e.g., Scambos et al., 2000). In our model, however, rapid disintegration could occur for grounded portions of the ice sheet. Even for modest values of ν, we anticipate that retreat could occur much more rapidly than would be simulated by models that assume Glen's flow law holds across all stress regimes. This potential progression of failure in deep retrograde beds is illustrated schematically in Figure 5.

7. Numerical Examples

### 7.1. Four Reduced Models of Calving Glaciers

Equations (45)–(49) and equations (54)–(56) provide a complete set of equations that specifies glacier evolution and terminus position. We illustrate the application of these equations for four limiting cases. The first model, which we call the 'Weertman' model, corresponds to equation (49) with the basal yield strength $T_b = 0$, resulting in the dynamic equation

$$2\delta \frac{\partial}{\partial x}\left(h|u_x|^{1/n-1}u_x\right) - \min\left(|u|^{m-1}, \frac{T_y}{|u|}\right)u = hs_x. \tag{58}$$

The second model, which we call the Plastic bed model, assumes that $T_y \gg T_b$, and hence, the shear stress at the bed is equal to the yield strength of ice everywhere, resulting in the dynamic equation

$$2\delta \frac{\partial}{\partial x}\left(h|u_x|^{1/n-1}u_x\right) - \frac{T_y}{|u|}u = hs_x. \tag{59}$$

These two models reduce further if $\delta \ll 1$. Our third model, which we call the SIA model, corresponds to $\delta \ll 1$ in the Weertman model. Dropping the term related to the longitudinal stress gradient and combining
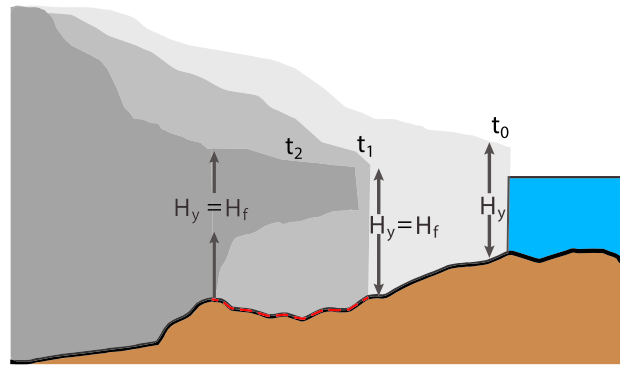
Figure 5. Conceptual illustration of the evolution of a glacier. Starting at the most advanced position (time t_0, light gray shaded profile), thinning of the glacier decreases the ice thickness. As the ice thickness at the terminus decreases, the calving front retreats to a position where the thickness can again reach the yield thickness (time t_2 medium shaded gray profile). If the glacier retreats into a deep trough, then the buoyancy thickness may exceed the yield thickness (illustrated with a dashed red line). In this case, the yielded rheology will result in rapid thinning (with the yielded rheology; equation (35)), a (nearly) instantaneous retreat of the grounding line to a position where the yield thickness can again be reached, and formation of a floating melange tongue (t_2, dark gray shaded profile).

with the ice thickness evolution equation provides the usual SIA diffusive equation for the glacier surface elevation:

$$h_t = \left(h^{1/m+1} |s_x|^{1/m-1} s_x \right)_x + \dot{a}, \quad |s_x| \leq \frac{T_y}{h}. \tag{60}$$

Our fourth model corresponds to $\delta \ll 1$ in the 'Plastic bed' model and reduces to the Perfect plastic approximation:

$$s_x = \pm \frac{T_y}{h}, \qquad u = \epsilon \left(\frac{1}{h(L)} \int_0^{x_L} (\dot{a} - h_t) \ dx \right). \tag{61}$$

For a discussion of numerical methods, we refer the reader to Appendix B.

7.2. Geometric Setting

We applied the calving parameterization defined by equation (54) to an idealized geometry motivated by Oerlemans (2008). The idealized glacial geometry assumes a glacier on a gently sloping bed with a Gaussian

Table 1
Numerical Values of Parameters Used in Different Models

Quantity	Value	Description
τ_y	150 kPa	Yield strength
B_i	10^8 Pa·s$^{-1/3}$	Hardness of intact ice
B_f	— Pa·s$^{-1/3}$	Hardness of failed ice
β	7.624×10^6 Pa·s/m	Sliding coefficient
m	1/3	Sliding law exponent
$\dot{a}_0$	0.75 m/a	Dimensional accumulation rate
Δa	1 m/a	Variation in accumulation rate
T	5,000 a	Period accumulation change
b_0	260 m	Bed elevation at $x = 0$
α	0.017	Bed slope
b_1	350 m	Height of bump in the bed
x_0	40 km	Center of bump in the bed
σ	10 km	Width of bump in the bed

Note. The hardness parameter of yielded ice is not used in any of the simulations.
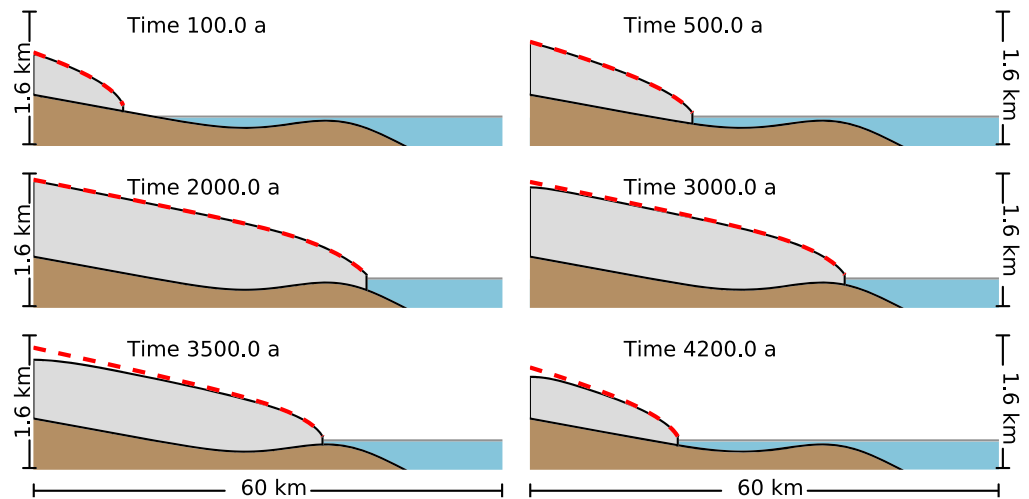
Figure 6. Snapshots showing advance and retreat for the plastic bed model (filled gray outline) and perfect plastic approximation (dashed red lines).

bump, representing a sill. In dimensional units, the bed takes the form:

$$b(x) = b_0 - \alpha x + b_1 \exp\left[-\left(\frac{x - x_0}{\sigma}\right)^2\right]. \tag{62}$$

Parameters follow Oerlemans (2008) and are provided in Table 1 in dimensional form.

7.3. Glacier Profiles

We first considered the temporal evolution of glaciers, including advance and retreat of the calving front. We assumed a slowly changing accumulation rate $\dot{a}$ of the form

$$\dot{a} = a_0 + \Delta a \sin\left(\frac{2\pi t}{T}\right). \tag{63}$$

In all calculations we assumed that ice at the terminus is at the yield strength and evolved the terminus according to equation (54). Figure 6 shows a sequence of snapshots illustrating glacier profiles constructed using the perfect plastic approximation and plastic bed model. For a given terminus position, differences between the perfect plastic and plastic bed profiles are largest upstream, away from the calving front. This pattern is a consequence of the Perfect plastic approximation neglecting deformation near the ice divide,
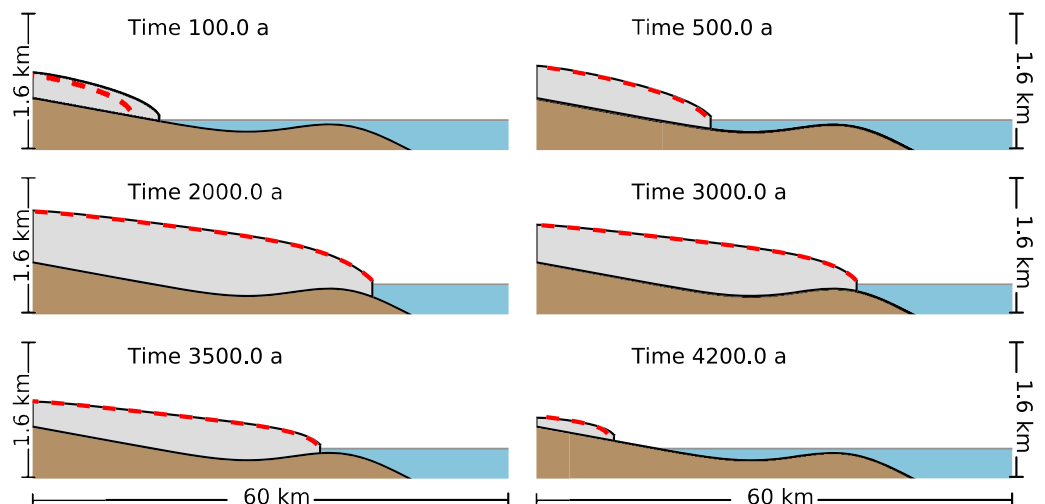
Figure 7. Snapshots showing advance and retreat for the Weertman model (filled gray outline) and shallow ice approximation model (dashed red lines).
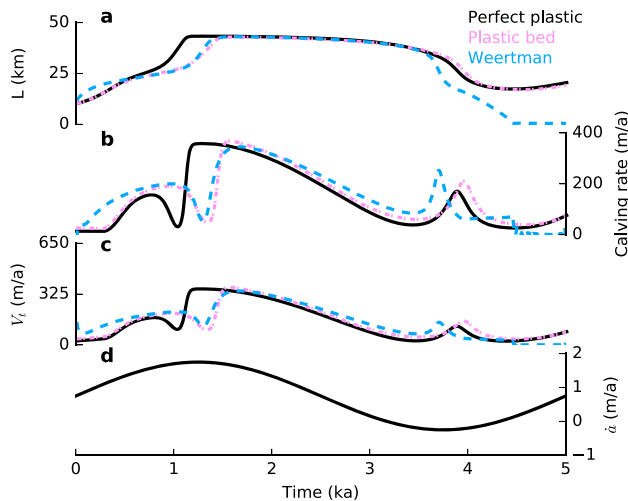
Figure 8. Time series showing the evolution of terminus position (a), calving rate (b), and terminus velocity (c) for a time-varying accumulation rate (d). The black line shows the trajectory based on the perfect plastic approximation model. The pink line shows the trajectory calculated using the plastic bed model, and the blue line shows the trajectory calculated using the Weertman model.

requiring a larger slope and producing a thicker glacier. Figure 7 shows an equivalent set of snapshots but this time comparing the Weertman model with the simpler boundary layer approximation defined by the SIA model. For the parameter regime used here, longitudinal stresses are small everywhere except near the calving front and the profiles are in close agreement. Differences between profiles are greatest early on when the glaciers are relatively small and deformational creep cannot be neglected.

Figure 8 shows a time series of glacier length, calving rate, and terminus velocity as the accumulation rate changes computed for (1) the perfect plastic, (2) plastic bed, and (3) Weertman models. (We omit the SIA model because the difference with the Weertman model is small.) Despite the slowly varying forcing, all three models exhibit sudden changes in terminus position that manifest as "spikes," analogous to the sudden retreat of real glaciers. In this case, the glacier responds slowly when its terminus is perched on a stable position on the sill. Retreat occurs rapidly when the glacier retreats (or advances) into an overdeepening, where ice thickness (and flux) rapidly increase. This is analogous to observations of rapid retreat when the bed is deep (e.g., Benn et al., 2007). The plastic bed, perfect plastic, and Weertman models predict advance rates and retreat rates that are broadly similar. However, the plastic bed and perfect plastic models are more stable to changes in accumulation rate and have a delayed retreat compared to the Weertman model.

7.4. Multiple Steady State and Hysteresis

Observations show that advance and retreat of tidewater glaciers can exhibit complex patterns that are not clearly synced with climate forcing (e.g., Pfeffer, 2003). To assess the ability of our suite of models to simulate a highly nonlinear response to climate, we computed stable steady-state terminus positions for the forcing previously considered. Figure 9 shows bifurcation diagrams illustrating stable and unstable terminus positions as a function of accumulation rate $\dot{a}$. We find three bifurcation points, with the first bifurcation point located near the coastline where the glacier first comes into contact with the ocean. The second and third bifurcation points occur at the deepest part of the overdeeping and the top of the sill, respectively. The positions of these bifurcation points are determined by the geometry of the glacier bed. Different sliding laws and choices of yield strength result in identical bifurcation points along the bed. This suggests that bed geometry controls the stable positions in which we observe glaciers. However, the sliding law controls climate sensitivity and the rates of retreat and advance.
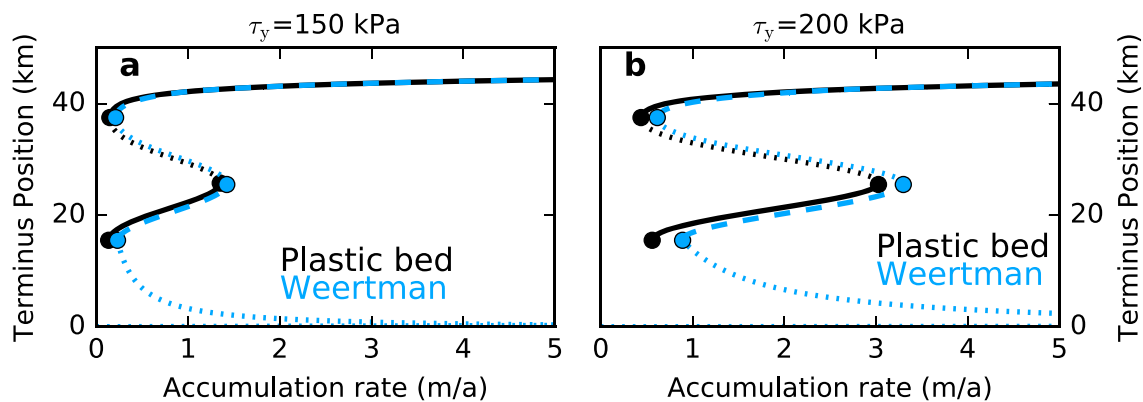
Figure 9. Bifurcation diagram showing terminus position as a function of accumulation rate for the plastic bed model (black) and Weertman model (blue). Stable solutions are indicated using a solid black line for the plastic bed model and dashed line for the Weertman model. Dotted lines show unstable branches. Circles denote bifurcation points where the solutions transition from stable to unstable. (a, b) Solutions obtained for a yield strength $\tau_y = 150$ kPa and $\tau_y = 200$ kPa, respectively.

8. Discussion

The thin film plastic approximation for glaciers developed here provides an avenue to simulate intact and fractured ice in a single modeling framework. Assuming that (i) the biviscious rheology of ice approximates real glacier flow, (ii) yielded ice flows much faster than intact ice, and (iii) the calving front is the boundary separating yielded from unyielded ice, we can bound the long-term calving rate and calving flux. This bound is independent of the rheology of failed ice provided that the yield thickness remains less than the flotation thickness. However, once a glacier retreats into an overdeepening bed where the flotation thickness exceeds the yield thickness, grounding line retreat will be paced by the rheology of the yielded ice mélange. Mélange rheology is poorly constrained (e.g., Robel, 2017), but it is likely much weaker than intact ice. Weak mélange opens the potential for ice sheet disintegration that proceeds much more rapidly than is possible with fully intact ice—a consequence already deduced by Weertman (1974) in his original treatment of the marine ice sheet instability. The mechanical simplifications we adopted do neglect bending and buckling stresses, which could be important near the calving front of glaciers. A more detailed treatment in the future may seek to include these effects—especially as glaciers approach buoyancy.

The idealized simulations that we conducted also display qualitatively realistic responses to climate forcing—including multiple steady states. Crucially, for the entire suite of glacier dynamic models considered, stable terminus positions are controlled by bed geometry. Near the most advanced position, we found that glaciers can exhibit remarkably little sensitivity to changes in climate forcing. However, once the climate forcing reaches a tipping point, retreat is irreversible unless the accumulation rate becomes significantly more positive. Although these results depend on the idealized geometry we assumed, most tidewater glaciers have a geometry that includes an overdeepening and sill. Thus, our results likely apply to more realistic geometries and may help explain the markedly different sensitivity of adjacent glaciers to changes in climate forcing.

Our model, although simplified, builds on the recently proposed marine ice cliff instability (Bassis & Walker, 2012; DeConto & Pollard, 2016). At least for two dimensions, where the maximum shear is equal to the effective stress, the bound on ice thickness we derived is identical to that proposed by Bassis and Walker (2012), with a factor of 2 errors in Bassis and Walker (2012) corrected. However, unlike Bassis and Walker (2012), which only provides a threshold on the maximum ice thickness permissible, our model is able to relate the ice thickness threshold to the rate of retreat possibly associated with the marine ice cliff instability. These bounds emerge from the assumption that the effective stress at the terminus must always be less than the yield strength of ice and only depend on a single parameter—the yield strength of ice. This should be contrasted with empirical calving law proposed by DeConto and Pollard (2016) that is based on retreat rates for Jakobshavn Isbræ and calibrated to match paleo ice sheet extents. Furthermore, our bound for retreat rates depends on the near-terminus geometry (ice thickness, bed slope, and ice thickness gradient), accumulation rate, and hardness of ice. A consequence is that our model predicts that glaciers with identical thickness may retreat at markedly different rates, depending on the geometric setting and climate forcing. This may help explain the observed breakdown in correlations between ice thickness and calving rates during glacier retreat (Van Der Veen, 1996) and agrees with observational evidence that geometry plays a dominant role in controlling calving rates (Catania et al., 2018; Enderlin et al., 2018).

Teasing out if our bound on calving rate holds for more realistic situations, however, requires a more thorough comparison of model predictions with observations using realistic geometry and forcing. We previously used a model similar to the SIA limit of the more general model developed here to successfully reproduce characteristics of Heinrich Events (Bassis et al., 2017), but this earlier study was highly idealized. Applying our model formalism to more realistic modern glacier configurations along with developing approximations that apply to two-dimensional (plan view) and fully three-dimensional models is a focus of current work.

9. Conclusions

We have developed a thin film viscoplastic model that encapsulates the flow of intact and yielded ice. Requiring that the effective stress within a glacier is bounded from above by the yield strength provides an upper bound on the ice thickness at the calving front (equation (47)). Remarkably, a bound on the long-term average rate of terminus advance emerges naturally as a consequence of the assumption that glacier ice cannot exceed the yield thickness (equation (52)). This approach differs from the current trends in ice dynamics in which the "fluid" part of dynamics is treated independently of the "fracture" component. In our model, the

evolution equation for terminus position emerges from the biviscous rheology as opposed to being imposed separately. This biviscous rheology provides a promising avenue to simulate the failure of glacier ice.

The calving rate evolution equation we derived provides a bound on calving fluxes and depends on a single additional parameter—the yield strength. Promisingly, the yield strength is a material property that can be constrained by field and laboratory measurements (e.g., Bassis & Walker, 2012; Vaughan, 1993). Furthermore, our model provides a simple theoretical framework to study the rapid retreat rates that recent studies (Bassis & Walker, 2012; Bassis et al., 2017; DeConto & Pollard, 2016) suggest may affect the West Antarctic Ice Sheet under calving cliff collapse.

Appendix A: Extensional Stress Boundary Layer in the Perfect Plastic Approximation

We return to the perfect plastic approximation continuing with the expansion and notation defined in section 5. Requiring a dominant balance between gradients in longitudinal stress and sliding when ice is at the yield strength at the bed suggests the rescaling

$$x - x_c = \epsilon^2 X, \quad s = \epsilon S, \quad h = \epsilon H, \quad b = \epsilon B, \quad \hat{u} = \epsilon^{-1} U. \tag{A1}$$

Following Schoof (2007), we also assume that the bed topography B only varies significantly on the "outer" length scale associated with the original horizontal coordinate x. With this rescaling, the strain rate components in the boundary layer become $\hat{u}_x = \epsilon^{-3} U_X$, $\hat{u}_z = \epsilon^{-2} U_Z$, which motivates the strain rate invariant rescaling

$$\hat{\dot{\gamma}} = \epsilon^{-3} E = \epsilon^{-3} \sqrt{U_X^2 + U_Z^2}. \tag{A2}$$

Assuming an expansion of the form $\hat{U} = \hat{U}_0(X, t) + \epsilon^2 \hat{U}_2(X, Z, t) + \ldots$, the leading order stress balance becomes

$$2 \left(H T_y \frac{\partial_X \hat{U}_0}{|\partial_X \hat{U}_0|} \right)_X - T_y \frac{\hat{U}_0}{|\hat{U}_0|} = H H_X, \tag{A3}$$

whereas the ice thickness evolution equation to order ϵ becomes

$$(H \hat{U}_0)_X = 0. \tag{A4}$$

Our boundary condition that vertical shear stress vanishes at $X = 0$ is now automatically satisfied, and the boundary condition on longitudinal stress becomes an ice thickness boundary condition

$$T_y = \frac{H}{4} \left(1 - \frac{\rho_w}{\rho} \frac{D^2}{H^2} \right). \tag{A5}$$

This equation can only be satisfied if the ice thickness at the calving front $H_c = H(0, t)$ is given by

$$H_c = H_y = 2T_y + \sqrt{\frac{\rho_w D^2}{\rho} + 4T_y^2}, \tag{A6}$$

where H_y is the required terminus thickness so the glacier is at the yield strength and we have discarded the unphysical negative square root.

Using the boundary condition on ice thickness at the terminus given by equation (A6), equation (A3) now can be explicitly integrated to find an expression for ice thickness in the boundary layer

$$H = 2T_y + \sqrt{4T_y^2 + \frac{\rho_w}{\rho} D^2 - 2T_y X}, \quad -\infty < X \le 0. \tag{A7}$$

In the limit $X \to -\infty$, $H \sim \sqrt{-2T_y X}$, we match equation (45) for ice thickness in the limit that the bed is flat. The flat bed condition, however, is exactly what we deduced is required in the boundary layer so long as bed topography varies on the outer length scale and the solutions match in the limit $x \to \infty$ and $X \to -\infty$.

Appendix B: Model Numerics

For the SSA-type models, we impose a symmetric boundary condition at the ice divide $s_x = 0$ and $u = 0$ at $x = 0$. For the SIA-type models we need to impose $s_x = 0$ at $x = 0$. For the perfect plastic model we need only specify the thickness at the terminus. To accurately resolve the terminus position, we adopt a moving grid. If the terminus position is located at $x_c(t)$, then defining

$$\xi = \frac{x}{x_c}, \quad \tilde{t} = t \tag{B1}$$

maps the interval $0 \leq x \leq x_c(t)$ into the interval $0 \leq \xi \leq 1$. The variable $\tilde{t}$ is introduced to distinguish between partial derivatives obtained holding x or ξ constant. Straightforward application of the chain rule then leads to

$$\frac{\partial}{\partial x} = \frac{1}{x_c} \frac{\partial}{\partial \xi}, \tag{B2}$$

$$\frac{\partial}{\partial t} = \frac{\partial}{\partial \tilde{t}} - \frac{\xi}{x_c} \frac{dx_c}{d\tilde{t}} \frac{\partial}{\partial \xi}. \tag{B3}$$

These transformations apply to all equations. To accurately resolve the boundary layer near the calving front, we use an unevenly spaced grid with points in the interval $[-1, 1]$ given by $\xi_j = 0.5 \cos(j\pi/N) + 0.5$, where N is the number of grid points and $0 \leq j \leq N$. The irregular grid spacing is accommodated using a finite element formulation with a basis set of "tent" functions that are defined to be unity at a single node and to vary linearly between nodes. To avoid numerical artifacts or resolution issues, we set $N = 1,600$ or higher.

References

Albrecht, T., & Levermann, A. (2012). Fracture field for large-scale ice dynamics. *Journal of Glaciology*, *58*(207), 165–176. https://doi.org/10.3189/2012JoG11J191

Astrom, J. A., Vallot, D., Schäfer, M., Welty, E. Z., O'Neel, S., Bartholomaus, T. C., et al. (2014). Termini of calving glaciers as self-organized critical systems. *Nature Geoscience*, *7*(12), 874–878. https://doi.org/10.1038/NGEO2290

Balmforth, N. J., & Craster, R. V. (1999). A consistent thin-layer theory for Bingham plastics. *Journal of Non-Newtonian Fluid Mechanics*, *84*(1), 65–81. https://doi.org/10.1016/S0377-0257(98)00133-5

Bassis, J. N. (2011). The statistical physics of iceberg calving and the emergence of universal calving laws. *Journal of Glaciology*, *57*(201), 3–16. https://doi.org/10.3189/002214311795306745

Bassis, J. N., & Jacobs, S. S. (2013). Diverse calving patterns linked to glacier geometry. *Nature Geoscience*, *6*(10), 833–836. https://doi.org/10.1038/NGEO1887

Bassis, J. N., & Ma, Y. (2015). Evolution of basal crevasses links ice shelf stability to ocean forcing. *Earth and Planetary Science Letters*, *409*, 203–211. https://doi.org/10.1016/j.epsl.2014.11.003

Bassis, J. N., Petersen, S. V., & Cathles, L. M. (2017). Heinrich events triggered by ocean forcing and modulated by isostatic adjustment. *Nature*, *542*, 332–334. https://doi.org/10.1038/nature21069

Bassis, J. N., & Walker, C. C. (2012). Upper and lower limits on the stability of calving glaciers from the yield strength envelope of ice. *Proceedings of the Royal Society A: Mathematical Physical and Engineering Science*, *468*(2140), 913–931. https://doi.org/10.1098/rspa.2011.0422

Benn, D. I., Warren, C. R., & Mottram, R. H. (2007). Calving processes and the dynamics of calving glaciers. *Earth-Science Reviews*, *82*(3-4), 143–179. https://doi.org/10.1016/j.earscirev.2007.02.002

Borstad, C., Khazendar, A., & Larour, E. (2012a). A damage mechanics assessment of the Larsen B ice shelf prior to collapse: Toward a physically-based calving law. *Geophysical Research Letters*, *39*, L11604. https://doi.org/10.1029/2012GL053317

Borstad, C. P., Khazendar, A., Larour, E., Morlighem, M., Rignot, E., Schodlok, M. P., & Seroussi, H. (2012b). A damage mechanics assessment of the Larsen B ice shelf prior to collapse: Toward a physically-based calving law. *Geophysical Research Letters*, *39*, L18502. https://doi.org/10.1029/2012GL053317

Borstad, C., Khazendar, A., Scheuchl, B., Morlighem, M., Larour, E., & Rignot, E. (2016). A constitutive framework for predicting weakening and reduced buttressing of ice shelves based on observations of the progressive deterioration of the remnant Larsen B Ice Shelf. *Geophysical Research Letters*, *43*, 2027–2035. https://doi.org/10.1002/2015GL067365

Catania, G. A., Stearns, L. A., Sutherland, D. A., Fried, M. J., Bartholomaus, T. C., Morlighem, M., et al. (2018). Geometric controls on tidewater glacier retreat in central western Greenland. *Journal of Geophysical Research: Earth Surface*, *123*, 2024–2038. https://doi.org/10.1029/2017JF004499

Cuffey, K., & Paterson, W. S. B. (1994). *The physics of glaciers* (3rd ed.). Oxford: Reed Educational and Professional Publishing Ltd.

Dahlen, F. A. (1990). Critical taper model of fold-and-thrust belts and accretionary wedges. *Annual Review of Earth and Planetary Sciences*, *18*(1), 55–99. https://doi.org/10.1146/annurev.ea.18.050190.000415

DeConto, R. M., & Pollard, D. (2016). Contribution of Antarctica to past and future sea-level rise. *Nature*, *531*(7596), 591–597. https://doi.org/10.1038/nature17145

Duddu, R., Bassis, J. N., & Waisman, H. (2013). A numerical investigation of surface crevasse propagation in glaciers using nonlocal continuum damage mechanics. *Geophysical Research Letters*, *40*, 3064–3068. https://doi.org/10.1002/grl.50602

Enderlin, E. M., O'Neel, S., Bartholomaus, T. C., & Joughin, I. (2018). Evolving environmental and geometric controls on Columbia glacier's continued retreat. *Journal of Geophysical Research: Earth Surface*, *123*, 1528–1545. https://doi.org/10.1029/2017JF004541

Greve, R., & Blatter, H. (2009). *Dynamics of ice sheets and glaciers*. Berlin: Springer. https://doi.org/10.1007/978-3-642-03415-2

Howat, I. M., Joughin, I., & Scambos, T. A. (2007). Rapid changes in ice discharge from Greenland outlet glaciers. *Science*, *315*(5818), 1559–1561. https://doi.org/10.1126/science.1138478

Howat, I. M., Joughin, I., Tulaczyk, S., & Gogineni, S. P. (2005). Rapid retreat and acceleration of Helheim Glacier, East Greenland. *Geophysical Research Letters*, *32*, L22502. https://doi.org/10.1029/2005GL024737

Joughin, I., Howat, I., Alley, R. B., Ekstrom, G., Fahnestock, M., Moon, T., et al. (2008). Ice-front variation and tidewater behavior on Helheim and Kangerdlugssuaq Glaciers, Greenland. *Journal of Geophysical Research*, *113*, F01004. https://doi.org/10.1029/2007JF000837

Krimmel, R. M. (2001). Photogrammetric data set, 1957-2000, and bathymetric measurements for Columbia Glacier Alaska (Tech. rep.): USGS.

McFadden, E. M., Howat, I. M., Joughin, I., Smith, B. E., & Ahn, Y. (2011). Changes in the dynamics of marine terminating outlet glaciers in west Greenland (2000–2009). *Journal of Geophysical Research*, *116*, F02022. https://doi.org/10.1029/2010JF001757

Mcnabb, R. W., Hock, R., O'Neel, S., Rasmussen, L. A., Ahn, Y., Braun, M., et al. (2012). Using surface velocities to calculate ice thickness and bed topography: A case study at Columbia Glacier, Alaska, USA. *Journal of Glaciology*, *58*(212), 1151–1164. https://doi.org/10.3189/2012JoG11J249

Meier, M. F., & Post, A. (1987). Fast tidewater glaciers. *Journal of Geophysical Research*, *92*(B9), 9051–9058. https://doi.org/10.1029/JB092iB09p09051

Moresi, L., Dufour, F., & Mühlhaus, H. B. (2003). A Lagrangian integration point finite element method for large deformation modeling of viscoelastic geomaterials. *Journal of Computational Physics*, *184*(2), 476–497. https://doi.org/10.1016/S0021-9991(02)00031-1

Murray, T., Selmes, N., James, T. D., Edwards, S., Martin, I., O'Farrell, T., et al. (2015). Dynamics of glacier calving at the ungrounded margin of Helheim Glacier, southeast Greenland. *Journal of Geophysical Research: Earth Surface*, *120*, 964–982. https://doi.org/10.1002/2015JF003531

Nick, F. M., Van der Veen, C. J., Vieli, A., & Benn, D. I. (2010). A physically based calving model applied to marine outlet glaciers and implications for the glacier dynamics. *Journal of Glaciology*, *56*(199), 781–794. https://doi.org/10.3189/002214310794457344

Nye, J. F. (1957). The distribution of stress and velocity in glaciers and ice-sheets. *Proceedings of the Royal Society of London. Series A. Mathematical and Physical Sciences*, *239*(1216), 113–133. https://doi.org/10.1098/rspa.1957.0026

O'Neel, S., Pfeffer, W. T., Krimmel, R., & Meier, M. (2005). Evolving force balance at Columbia Glacier, Alaska, during its rapid retreat. *Journal of Geophysical Research*, *110*, F03012. https://doi.org/10.1029/2005JF000292

O'Neill, C., Moresi, L., Müller, D., Albert, R., & Dufour, F. (2006). Ellipsis 3D: A particle-in-cell finite-element hybrid code for modelling mantle convection and lithospheric deformation. *Computers & Geosciences*, *32*(10), 1769–1779. https://doi.org/10.1016/j.cageo.2006.04.006

Oerlemans, J. (2008). *Minimal glacier models*. Universiteitsbibliotheek Utrecht: Igitur.

Pfeffer, W. T. (2003). Tidewater glaciers move at their own pace. *Nature*, *426*(6967), 602. https://doi.org/10.1038/426602b

Pralong, A., & Funk, M. (2005). Dynamic damage model of crevasse opening and application to glacier calving. *Journal of Geophysical Research*, *110*, B01309. https://doi.org/10.1029/2004JB003104

Rignot, E., Velicogna, I., van den Broeke, M. R., Monaghan, A., & Lenaerts, J. T. M. (2011). Acceleration of the contribution of the Greenland and Antarctic ice sheets to sea level rise. *Geophysical Research Letters*, *38*, L05503. https://doi.org/10.1029/2011GL046583

Rist, M. A., Sammonds, P. R., Oerter, H., & Doake, C. S. M. (2002). Fracture of Antarctic shelf ice. *Journal of Geophysical Research*, *107*(B1), 2002–2002. https://doi.org/10.1029/2000JB000058

Robel, A. A. (2017). Thinning sea ice weakens buttressing force of iceberg mélange and promotes calving. *Nature Communications*, *8*(14), 596. https://doi.org/10.1038/ncomms14596

Scambos, T. A., Hulbe, C., Fahnestock, M., & Bohlander, J. (2000). The link between climate warming and break-up of ice shelves in the Antarctic Peninsula. *Journal of Glaciology*, *46*, 516–530. https://doi.org/10.3189/172756500781833043

Schoof, C. (2007). Marine ice-sheet dynamics. Part 1. The case of rapid sliding. *Journal of Fluid Mechanics*, *573*, 27–55. https://doi.org/10.1017/S0022112006003570

Schulson, E. M. (2001). Brittle failure of ice. *Engineering Fracture Mechancis*, *68*(17), 1839–1887. https://doi.org/10.1016/S0013-7944(01)00037-6

Schulson, E. M., & Duval, P. (2009). *Creep and fracture of ice*. Cambridge: Cambridge University Press. https://doi.org/10.3189/S0022143000206254

Straneo, F., Heimbach, P., Sergienko, O., Hamilton, G., Catania, G., Griffies, S., et al. (2013). Challenges to understanding the dynamic response of Greenland's marine terminating glaciers to oceanic and atmospheric forcing. *Bulletin of the American Meteorological Society*, *94*(8), 1131–1144. https://doi.org/10.1175/BAMS-D-12-00100.1

Thomas, R. (1977). Calving bay dynamics and ice sheet retreat up the St Lawrence Valley system. *Gé,ographie physique et Quaternaire*, *31*(3-4), 347–356. https://doi.org/10.7202/1000282ar

Ultee, L., & Bassis, J. (2016). The future is Nye: An extension of the perfect plastic approximation to tidewater glaciers. *Journal of Glaciology*, *62*(236), 1143–1152. https://doi.org/10.1017/jog.2016.108

Van Der Veen, C. J. (1996). Tidewater calving. *Journal of Glaciology*, *42*(141), 375–385. https://doi.org/10.3189/S0022143000004226

Van der Veen, C. J. (1999). *Fundamentals of glacier dynamics*. Boca Raton: CRC Press.

Vaughan, D. G. (1993). Relating the occurrence of crevasses to surface strain rates. *Journal of Glaciology*, *39*(132), 255–266. https://doi.org/10.3189/S0022143000015926

Weertman, J. (1974). Stability of the junction of an ice sheet and an ice shelf. *Journal of Glaciology*, *13*(67), 3–11. https://doi.org/10.3189/S0022143000023327

Weertman, J. (1980). Bottom crevasses. *Journal of Glaciology*, *25*(91), 185–88. https://doi.org/10.3189/S0022143000010418